Gapped ground state in the zigzag pseudospin-1/2 quantum antiferromagnetic chain compound PrTiNbO6

Yuesheng Li, Sebastian Bachus, Yoshifumi Tokiwa, Alexander A. Tsirlin, Philipp Gegenwart

Gapped ground state in the zigzag pseudospin-1/2 quantum antiferromagnetic chain compound PrTiNbO$_6$

Yuesheng Li,[*] Sebastian Bachus, Yoshifumi Tokiwa, Alexander A. Tsirlin, and Philipp Gegenwart

Experimental Physics VI, Center for Electronic Correlations and Magnetism, University of Augsburg, 86159 Augsburg, Germany

We report a single-crystal study on the magnetism of the rare-earth compound PrTiNbO$_6$ that experimentally realizes the zigzag pseudospin-1/2 quantum antiferromagnetic chain model. Random crystal electric field caused by the site mixing between nonmagnetic Ti^{4+} and Nb^{5+} results in the non-Kramers ground-state quasidoublet of Pr^{3+} with the effective pseudospin-1/2 Ising moment. Despite the antiferromagnetic intersite coupling of about 4 K, no magnetic freezing is detected down to 0.1 K, while the system approaches its ground state with almost zero residual spin entropy. At low temperatures, a sizable gap of about 1 K is observed in zero field. We ascribe this gap to off-diagonal anisotropy terms in the pseudospin Hamiltonian, and argue that rare-earth oxides open an interesting venue for studying magnetism of quantum spin chains.

I. INTRODUCTION

One-dimensional (1D) $S = 1/2$ quantum spin chains (QSC) have captured extensive interest of both theorists and experimentalists for almost 100 years. Strong quantum fluctuations are integral to such systems, owing to their low dimensionality, low coordination number, and low spin. Abundant novel states of matter, including "quantum spin liquid" (QSL) phases named Luttinger liquids in the purely 1D case, may occur [1–6]. QSC is a basic model, which in special cases can even be solved exactly [7]. It is well known that the $S = 1/2$ antiferromagnetical Heisenberg spin chain with only nearest-neighbor (NN) interactions has no long-range order and exhibits a gapless energy spectrum according to the Lieb-Schultz-Mattis theorem [7]. Magnetic excitations of this model can be represented by pairs of *spinons* carrying spin-1/2 each [2]. When Heisenberg interactions decaying as $1/r^2$ are added beyond NN, a gapless resonating-valence-bond ground state (GS) is expected [8]. In the presence of the XXZ anisotropy, a quantum-critical and gapless Luttinger liquid has been identified for a large (easy-plane) parameter region [9–12].

On the experimental side, many of the transition-metal compounds manifest different flavors of the QSC physics. Exchange couplings in these compounds can be isotropic, as in Sr$_2$CuO$_3$ (SrCuO$_2$) [13,14], Cu^{2+} molecular magnets [15], CuGeO$_3$ [16], and NaTiSi$_2$O$_6$ (LiTiSi$_2$O$_6$) [17], or anisotropic, as in several spin-chain Co^{2+} oxides with the strong easy-axis anisotropy [18–25]. Most of such compounds are magnetically ordered at low temperatures [13–15,18–25]. The delocalization of the 3d electrons causes non-negligible interchain interactions $J_\perp$ that eventually stabilize a long-range-ordered GS [13,26].

Recent studies uncovered the diverse and hitherto largely unexplored magnetism of 4f oxides. For example, we reported a triangular QSL candidate YbMgGaO$_4$ [27–31], where NN magnetic couplings are highly anisotropic in spin space and trigger new physics beyond that of the conventional XXZ model [32]. Moreover, localized nature of the 4f electrons renders long-range couplings diminutively small and enhances low dimensionality. Following the same idea, we seek to arrange rare-earth ions along a zigzag chain, arriving at a quasi-1D antiferromagnet with highly anisotropic intrachain and vanishingly small interchain couplings.

In this paper, we report a comprehensive study of the low-T magnetic properties of the rare-earth zigzag QSC single crystal PrTiNbO$_6$. Random crystal electric field (CEF) caused by the site mixing between nonmagnetic Ti^{4+} and Nb^{5+} results in the non-Kramers GS of Pr^{3+}, a quasidoublet with the effective pseudospin-1/2 moment and Ising anisotropy. No conventional spin freezing is detected down to 0.1 K, where residual entropy is close to zero, and the system approaches its GS. A sizable energy gap just above the GS is clearly detected, and its possible origin is discussed.

II. EXPERIMENTAL DETAILS

Polycrystalline samples of Pr$_x$La$_{1-x}$TiNbO$_6$ ($x = 1$, 0.5, 0.2, 0.08, 0.04, and 0) were synthesized by the traditional solid-state method. Large single crystals of PrTiNbO$_6$ [~1 cm, see Fig. 1(a)] were grown by the optical floating zone technique (see Appendix A). No measurable conductance of the sample was detected at room temperature for PrTiNbO$_6$.

The direct and alternating current (ac) magnetization ($1.8 \leqslant T \leqslant 400$ K, $0 \leqslant \mu_0H \leqslant 7$ T, and $7.57 \leqslant \nu \leqslant 757$ Hz) was measured by a magnetic property measurement system (MPMS, Quantum Design) using a 59.77 mg single crystal. The dc magnetization up to 14 T was measured by a vibrating sample magnetometer in a physical property measurement system (PPMS, Quantum Design).

The heat capacity ($0.36 \leqslant T \leqslant 400$ K and $0 \leqslant \mu_0H \leqslant 10$ T) was measured using cold-pressed powders (~10 mg), as well as a small single crystal of PrTiNbO$_6$ (5.37 mg) at 0 T, in a PPMS. N-grease was used to facilitate thermal contact
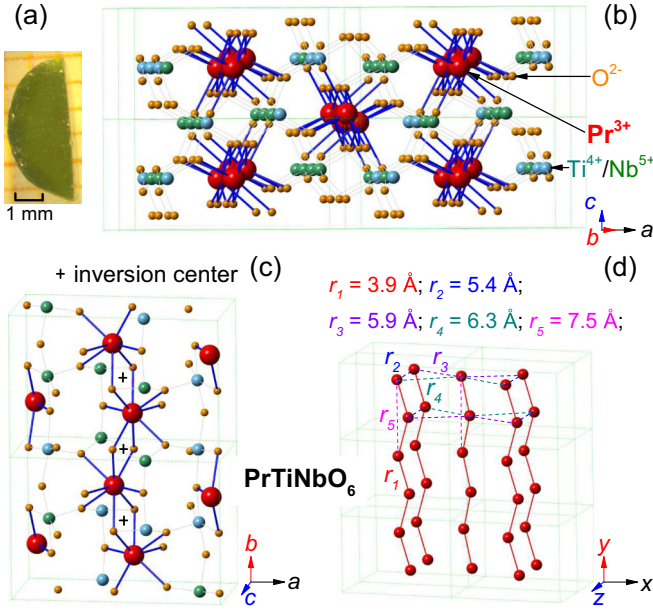
———————
*yuesheng.man.li@gmail.com

FIG. 1. (a) A typical as-grown single crystal of PrTiNbO$_6$. (b) View along the Pr^{3+} chain (b axis) of the crystal structure. (c) Zoom-in view of the Pr^{3+} chain in the ab plane. (d) Schematic plot for the Pr^{3+} chains. Ti^{4+}, Nb^{5+}, and O^{2-} are omitted for clarity, and the coordinate system for the spin components is defined in the inset. The NN Pr-Pr distance $r_1 = 3.9$ Å is comparable to the shortest Yb-Yb distance of 3.4 Å in YbMgGaO$_4$ [27,28]. The green dashed lines mark the unit cells.

between the sample and the puck below 210 K, while H-grease was used above 200 K. The sample coupling was better than 95%. The contributions of the grease and puck under different external fields were measured independently and subtracted from the data. The low temperatures down to 0.36 K were achieved by a ^{3}He refrigerator. The low-T heat capacity of the PrTiNbO$_6$ single crystal down to 0.09 K was measured in a home-built setup installed in a ^{3}He-^{4}He dilution refrigerator at external magnetic fields up to 0.8 T applied along the c axis. No significant sample dependence of the thermodynamic properties was observed for both powders and single crystals of PrTiNbO$_6$ [see Figs. 2(a) and 2(b)].

The setup for the milli-Kelvin heat capacity measurements is shown in the inset of Fig. 3(b) [33]. The single-crystal sample used in the measurement was cut into a small thin plate (5.37 mg). Its largest face was well polished and contacted to the platform using grease. Thermal link to the bath was achieved by a bronze wire of appropriate diameter and length to produce quasiadiabatic conditions. Thermal relaxation was analyzed using the two-τ model similar to Ref. [34],

$$P_h(t) = C_{pl} \frac{dT_{pl}}{dt} + K_g[T_{pl}(t) - T_{sa}(t)],$$

$$K_g[T_{pl}(t) - T_{sa}(t)] = C_{sa} \frac{dT_{sa}}{dt} + K_w[T_{sa}(t) - T_{ba}], \quad (1)$$

where C_{pl} and C_{sa} are the heat capacities of the platform and sample, respectively, K_g is the thermal conductance between the two, K_w is the thermal conductance of the thermal link, T_{pl}, T_{sa}, and T_{ba} are the temperatures of the platform, the sample,

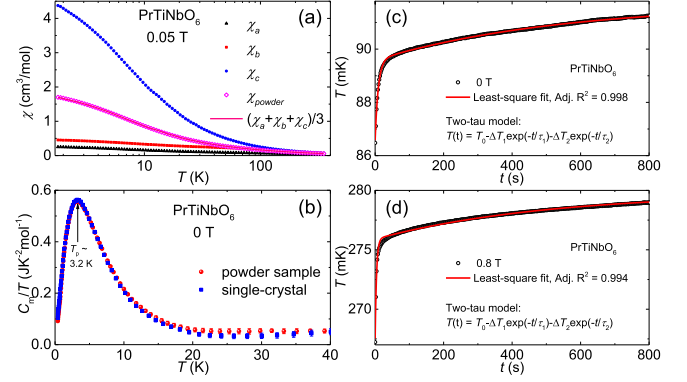FIG. 2. (a) Temperature dependence of the magnetic susceptibilities for both single crystal (along the a, b, and c axes) and powder of PrTiNbO$_6$, measured in an applied magnetic field of 0.05 T down to 1.8 K. (b) Low-T magnetic heat capacities measured for both single-crystal and powder samples of PrTiNbO$_6$ under zero field. Relaxation curves of the PrTiNbO$_6$ single crystal measured (c) at 0 T and (d) at 0.8 T applied along the c axis, with the red lines showing the corresponding least-square fits using the two-τ model.

and the thermal bath, respectively, and $P_h(t)$ is the power of the heater. The solution to the model takes the form

$$T_{sa}(t) = T_0 - \Delta T_1 e^{-t/\tau_1} - \Delta T_2 e^{-t/\tau_2}. \quad (2)$$

The experimental data can be fitted using Eq. (2) with five independent variables, T_0, ΔT_1, ΔT_1, τ_1, and τ_2 [see Figs. 2(c) and 2(d)]. Below 2 K, the background heat capacity ($\sim C_{pl}$) was negligible, $C_{pl} \sim 0.01$ μJ K^{-1} $< 0.03 C_{sa}$. Thus, we can obtain
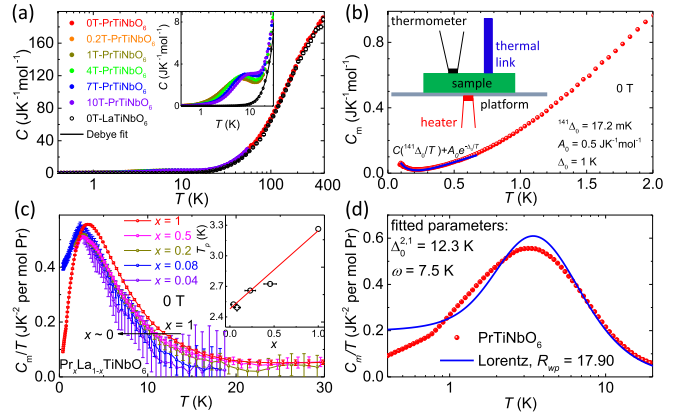

FIG. 3. (a) Heat capacities measured on the powders of PrTiNbO$_6$ and LaTiNbO$_6$ down to 0.4 K under different magnetic fields. The black curve presents a Debye fit to the heat capacity of LaTiNbO$_6$ below 50 K with the fitted Debye temperature $\sim$260 K. The inset shows a zoom-in view of the low-T data. (b) Low-T magnetic heat capacities of PrTiNbO$_6$ measured at 0 T down to 0.09 K. The blue curve shows the fit below 0.7 K with the fitted parameters shown in the figure. The inset shows the schematic view of the platform used for the milli-Kelvin heat capacity measurement. (c) Magnetic heat capacity measured on the Pr$_x$La$_{1-x}$TiNbO$_6$ ($x = 1$, 0.5, 0.2, 0.08, and 0.04) powders. The inset shows the x dependence of the peak position of the hump (T_p), with the red line representing a linear fit. (d) Magnetic heat capacity measured on PrTiNbO$_6$ with the blue line showing the least-R_{wp} fit with the Lorentzian distribution of E_2-E_1.

the temperature and heat capacity as $T = T_0 - \Delta T_1/2 - \Delta T_2/2$ and $C_{sa} = P(\tau_1 + \tau_2)/(\Delta T_1 + \Delta T_2)$, respectively, according to Eq. (1). Here P is the power increase of the heater.

At low temperatures, the nuclear contribution becomes dominant (see below), and the experimental data slightly deviate from the two-τ model at $\sim$30 s [see Fig. 2(c)]. At higher applied fields, the deviations occur even at higher temperatures [see Fig. 2(d) for example]. This deviation may be caused by the thermal decoupling between the phonon (lattice) and electronic/nuclear subsystems [35]. To avoid errors in the resulting heat capacity, we chose to exclude the heat capacity data with the adj. R^2 [36] smaller than 0.998 [see Fig. 2(d) for example]. Therefore, our zero-field data can extend to the lowest temperature of 0.09 K, whereas the data obtained in nonzero magnetic fields terminate at higher temperatures. This is because the applied magnetic field increases the nuclear gap due to Zeeman effect, and the nuclear contribution to the heat capacity shifts to higher temperatures. It also serves as a probe of the local magnetization, see Sec. III E for further analysis.

III. RESULTS AND DISCUSSION

A. Crystal structure

PrTiNbO$_6$ belongs to the family of RTiNbO$_6$ oxides (R = La, Ce, Pr, Nd, and Sm) with the space group *Pnma* (see Fig. 1). This family has been extensively studied due to the promising applications in ceramic microwave resonators and miniature solid-state laser systems [37–41]. However, its low-T magnetism was not reported to date.

The superexchange coupling between the NN Pr^{3+} ions (Wyckoff position, $4c$) is mediated by two parallel anions O^{2-}(2) ($8d$) along the zigzag chain (see Fig. 1 and Appendix A). Large spatial separation between the chains renders the magnetism quasi-1D [see Fig. 1(b)]. Assuming dipole-dipole nature of long-range couplings, we estimate the interchain interaction $J_\perp \lesssim \mu_0 \mu_B^2 g_c^2/(16\pi r_2^3) \sim 0.02$ K, and the next-nearest-neighbor intrachain interaction $J_2 \lesssim \mu_0 \mu_B^2 g_c^2/(16\pi r_5^3) \sim 0.006$ K, whereas the NN intrachain coupling is about 4 K, as we show below.

The site mixing between the magnetic and nonmagnetic ions is unlikely due to the large chemical differences between Pr^{3+} with the ionic radius $r_{Pr^{3+}} = 0.99$ Å and Ti^{4+}/Nb^{5+} ions with $r_{Ti^{4+}/Nb^{5+}} = 0.61/0.64$ Å [27]. On the other hand, Ti^{4+} and Nb^{5+} are statistically distributed in the structure. Our x-ray diffraction data confirm the statistical mixing and the absence of any superstructure reflections (see Fig. 8). No Pr^{3+} defects were detected either.

In the PrTiNbO$_6$ structure, inversion centers located halfway between the Pr^{3+} ions [see Fig. 1(c)] exclude the antisymmetric Dzyaloshinsky-Moriya interactions [27,42]. This renders PrTiNbO$_6$ a promising system for studying 1D anisotropic magnetism in the zigzag-chain geometry.

B. Crystal-field randomness and the ground-state quasidoublet

An isolated Pr^{3+} ion with the electronic configuration $4f^2$ forms the ninefold-degenerate GS, $|m_J\rangle$ ($m_J = \pm 4, \pm 3, \pm 2, \pm 1, 0$), with the spin angular momentum $s = 1$, orbital angular momentum $L = 5$, and total angular momentum $J = 4$, according to Hund's rules. In PrTiNbO$_6$, the C_{1h}
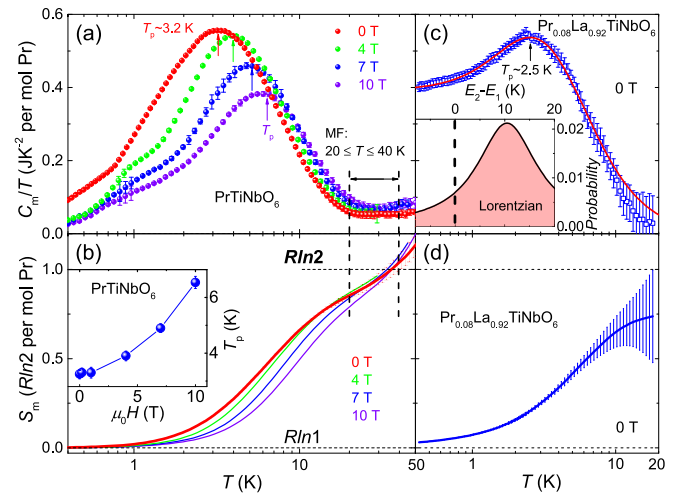

FIG. 4. (a) Magnetic heat capacity of the PrTiNbO$_6$ powder measured under external magnetic fields. The hump center temperatures (T_p) are marked. (b) Magnetic entropy of PrTiNbO$_6$. The inset shows the field dependence of T_p. (c) Magnetic heat capacity of the Pr$_{0.08}$La$_{0.92}$TiNbO$_6$ powder, with the red line showing the Lorentz fit. The inset represents the resulting Lorentzian distribution of E_2-E_1 with the fitted parameters $\Delta_0^{2,1} = 10.5$ K (center) and $\omega = 15$ K (width). (d) Magnetic entropy of Pr$_{0.08}$La$_{0.92}$TiNbO$_6$.

point-group symmetry of the Pr^{3+} site splits this GS into nine singlets.

The magnetic heat capacity (C_m) of PrTiNbO$_6$ can be determined very accurately by subtracting the heat capacity of the nonmagnetic LaTiNbO$_6$ as phonon contribution [see Fig. 3(a)]. At 0.4 K, the magnetic heat capacity of PrTiNbO$_6$ is extremely small, $C_m = 0.006 R \ln 2$, suggesting that the ground-state regime has been reached. At higher temperatures, a broad hump of C_m/T centered at $T_p \sim 3.2$ K is observed. By integrating C_m/T [Fig. 4(a)] over T, we obtain the magnetic entropy [Fig. 4(b)] that sharply increases in the vicinity of T_p. The curve flattens out around 40 K, where the value of $R \ln 2$ is reached. At higher temperatures, the entropy increases again due to the population of higher-lying CEF levels.

The nature of the magnetic entropy can be twofold. The CEF excitations between the two lowest-lying CEF singlets (single-ion magnetism) on one hand and the intersite magnetic interactions (cooperative magnetism) on the other hand, both contribute to the heat capacity and produce the total entropy of $R \ln 2$. To distinguish between these effects, we measured heat capacity of the magnetically diluted samples Pr$_x$La$_{1-x}$TiNbO$_6$. At $x = 0.04$, where intersite interactions should be fully suppressed, the entire hump is gradually shifted to a lower temperature of $\sim$2.5 K [see Fig. 3(c)]. However, we were unable to describe this hump assuming excitations between the two lowest CEF singlets, $|E_1\rangle$ and $|E_2\rangle$.

In a two-level system,

$$C_m^{CEF} = R \int p\left(E_2 - E_1 - \Delta_0^{2,1}\right)\left(\frac{E_2 - E_1}{T}\right)^2$$

$$\times \frac{e^{\frac{|E_2 - E_1|}{T}}}{\left(1 + e^{\frac{|E_2 - E_1|}{T}}\right)^2} d(E_2 - E_1), \quad (3)$$

where $p(E_2 - E_1 - \Delta_0^{2,1}) = \delta(E_2 - E_1 - \Delta_0^{2,1})$ is the spectral weight distribution function for the two-level model, $\Delta_0^{2,1}$ is the energy gap center, and $(E_2 - E_1)$ is the integration variable. The fit quality is assessed using

$$R_{wp} = \sqrt{\frac{1}{N} \sum_{j=1}^{N} \left(\frac{Y_j^{\text{obs}} - Y_j^{\text{cal}}}{\sigma_j^{\text{obs}}} \right)^2}, \qquad (4)$$

resulting in very high values $R_{wp} = 21$ and 6.4 for $x = 0.08$ and 0.04, respectively. Here Y_j^{obs} is the observed value, σ_j^{obs} is its standard deviation, and N is the number of the data points, whereas Y_j^{cal} is the calculated value. Indeed, the finite value of $C_m/T \sim 0.4 \, \text{J K}^{-2}$ per mol Pr at 0.4 K [see Fig. 4(c)] would not be possible in a two-level system, because such a system is necessarily gapped.

In YbMgGaO$_4$, a complete site mixing between Mg^{2+} and Ga^{3+} was reported to generate random electric fields on the Yb^{3+} ions and produce a broad distribution of the CEF levels. This distribution has the Lorentzian width of about 5 meV, as probed by inelastic neutron scattering [30]. A similar effect should take place in the RTiNbO$_6$ family, where the complete site mixing between Ti^{4+} and Nb^{5+} [37–41] generates random electric fields on the rare-earth sites. Taking this possibility into account, we modeled the heat capacity of the diluted samples assuming a Lorentzian distribution of the CEF excitation energy $E_2 - E_1$,

$$p\left(E_2 - E_1 - \Delta_0^{2,1}\right) = \frac{2}{\pi} \frac{\omega}{4\left(E_2 - E_1 - \Delta_0^{2,1}\right)^2 + \omega^2}. \qquad (5)$$

A perfect fit of the data for Pr$_{0.08}$La$_{0.92}$TiNbO$_6$ ($R_{wp} = 0.38$) yields the maximum of the distribution at $\Delta_0^{2,1} = 10.5$ K and the width $\omega = 15$ K [see Fig. 4(c)]. With $\omega > \Delta_0^{2,1}$, an accidental degeneracy of $|E_1\rangle$ and $|E_2\rangle$ occurs, and even at 0.4 K the heat capacity remains finite. A similar fit of the data for Pr$_{0.04}$La$_{0.96}$TiNbO$_6$ ($R_{wp} = 0.52$) produced nearly the same parameters, $\Delta_0^{2,1} = 10.3$ K and $\omega = 17$ K (see Appendix B), thus confirming that the mixing of Pr^{3+} and La^{3+} has minor effect on the CEF levels. In contrast to Ti^{4+} and Nb^{5+}, the La^{3+} and Pr^{3+} ions have the same point charge along with similar ionic radii. Therefore, they should not cause any significant changes in the local electric field environment of Pr^{3+}. Note also that in YbMgGaO$_4$ charge misbalance due to the mixing of differently charged ions, Mg^{2+} and Ga^{3+}, is the main cause for local structural distortions and the ensuing CEF randomness [30].

The picture emerging so far is that of a rather unexpected but mundane single-ion CEF physics. A striking observation is that the undiluted sample PrTiNbO$_6$ features a much lower heat capacity at 0.4 K compared to the diluted sample with $x = 0.08$. This leads us to conclude that the two lowest CEF states mix into a quasidoublet, $|\sigma_\pm\rangle = \frac{1}{\sqrt{2}}(|E_1\rangle \pm |E_2\rangle)$, and render Pr^{3+} a pseudospin-1/2 magnetic ion. Interactions between such ions open a gap and reduce the low-T heat capacity with respect to its single-ion value, compare Figs. 4(a) and 4(c). On the other hand, we were unable to fit the data for the undiluted sample using the single-ion CEF model, either without or with the CEF randomness [see Fig. 3(d)].
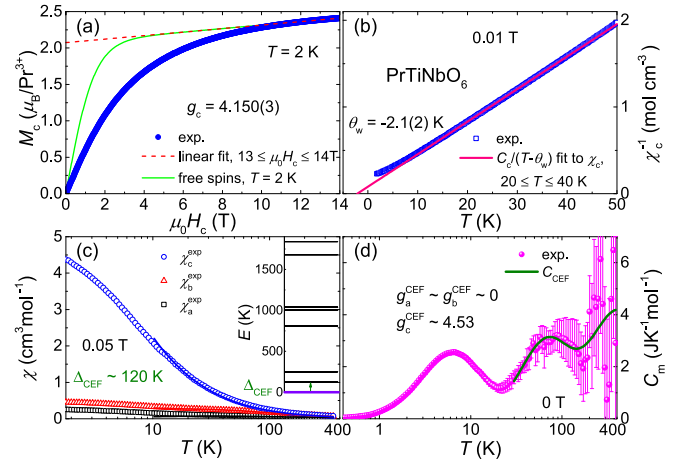

FIG. 5. (a) Magnetization of the PrTiNbO$_6$ single crystal measured along the c axis at 2 K. The red dashed line shows the linear fit to the data from 13 to 14 T, and the green line represents the calculation for the Pr^{3+} spins without intersite couplings. (b) Inverse magnetic susceptibility measured in the field of 0.01 T along the c axis. The red line shows the Curie-Weiss fit from 20 to 40 K. Combined CEF fit to both (c) susceptibilities (along the a, b, and c axes) and (d) heat capacity above 30 K. The inset of (c) shows the resulting CEF energy levels with the GS quasidoublet (violet line) and seven excited singlets (black lines).

Further fingerprints of the intersite interactions between such magnetic entities are seen in the magnetization data. At 2 K and above $\sim$10 T, the magnetization shows full polarization only along the c axis with a pseudospin-1/2 g factor, $g_c \sim 4.15$, and a very small Van Vleck susceptibility $\chi_c^{\text{vv}} \sim 0.16 \, \text{cm}^3/\text{mol}$ [see Fig. 5(a)]. The magnetization along the a or b axis, M_a or M_b, is proportional to the applied magnetic field up to 7 T [see Fig. 6(c)]. It was not possible to measure M_a and M_b in much higher applied fields, as the strong field broke the sample due to the strong magnetic anisotropy [inset of Fig. 6(c)]. Because C_m/T reaches a minimum between 20 and 40 K [see Fig. 4(a)], both the intersite spin-spin correlations and CEF excitations have marginal effect in this temperature range, and it can be used for the Curie-Weiss fitting. We thus obtained $\theta_w = -2.1(2)$ K, and the effective moment of $\mu_{\text{eff}} = 2.37(2) \, \mu_B \sim \frac{g_c}{2} \, \mu_B$ [see Fig. 5(b)]. Therefore, the intersite coupling is clearly antiferromagnetic, $J_{zz} = -2\theta_w \sim 4$ K, as further confirmed by modeling the magnetization at 2 K, where strong deviations from the magnetization process of an uncoupled Pr^{3+} entity are observed [see Fig. 5(a)].

Below T_p, the susceptibility χ_c is lower than predicted by the Curie-Weiss law [see Fig. 5(b)], suggesting that intersite antiferromagnetic correlations set in. The value of T_p increases with the applied magnetic field [see Fig. 4(b)], similar to YbMgGaO$_4$ [27]. Furthermore, the ac susceptibility shows no frequency dependence down to 1.8 K, thus excluding spin freezing below T_p (see Fig. 6).

C. CEF Hamiltonian

In order to probe higher-lying CEF states, we use the generic CEF Hamiltonian with the C_{1h} symmetry [43–45] and, for simplicity, exclude the CEF randomness. The data are fitted
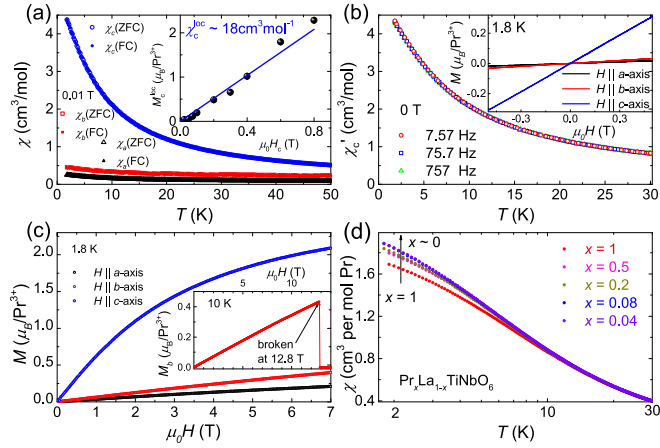
FIG. 6. (a) Magnetic susceptibilities measured under zero-field cooling (ZFC) and field cooling (FC) down to 1.8 K for the single crystal of $PrTiNbO_6$ along the a, b, and c axes. The inset represents the local magnetization extracted from the low-T heat capacity with the blue line showing a linear fit. (b) ac susceptibilities measured for the single crystal of $PrTiNbO_6$ along the c axis under zero field down to 1.8 K. The inset shows the complete magnetization loops measured at 1.8 K along the a, b, and c axes. (c) Field dependence of the magnetization measured at 1.8 K along the a, b, and c axes. The inset shows the magnetization along the b axis at 10 K up to 12.8 T. (d) Magnetic susceptibility of the $Pr_xLa_{1-x}TiNbO_6$ powders ($x = 1$, 0.5, 0.2, 0.08, and 0.04).

above 30 K, where effects of mixing between the two lowest states and of intersite correlations are excluded. We performed a combined single-ion CEF fit (see Appendix C) to χ_a, χ_b, χ_c [Fig. 5(c)], and C_m [Fig. 5(d)] taking into account the pseudospin-1/2 g-factors ($g_a = g_b = 0$, $g_c \sim 4.15$) from the magnetization data, and $\langle E_2 - E_1 \rangle \sim 10$ K [see Fig. 4(c)]. The third CEF level is found at $\Delta_{CEF} \sim 120$ K above the GS quasidoublet.

D. Effective pseudospin-1/2 Hamiltonian

At low temperatures, the formation of the pseudospin-1/2 quasidoublet with the strong Ising anisotropy [46] resembles non-Kramers GS doublets in the 3D pyrochlore compounds $Pr_2TM_2O_7$ (TM = Sn, Zr, Hf, and Ir), where Ising anisotropy had been reported too [47–51]. It is thus logical to use a similar NN pseudospin-1/2 Hamiltonian for interactions along the zigzag chain. The projection of the dominant NN superexchange interaction through the virtual fpf hopping process [52–54] onto the subspace of the GS CEF quasidoublet ($|\sigma_\pm\rangle$) results in

$$\mathcal{H} = \sum_{k=1}^{\infty} \big[J_{zz} S_k^z S_{k+1}^z + J_\pm (S_k^+ S_{k+1}^- + S_k^- S_{k+1}^+)$$
$$+ J_{\pm\pm}(S_k^+ S_{k+1}^+ + S_k^- S_{k+1}^-)$$
$$+ i^{2k+1} J'_{\pm\pm}(S_k^+ S_{k+1}^+ - S_k^- S_{k+1}^-) \big], \quad (6)$$

with the time-reversal invariant quadrupole moment $S_k^\pm \equiv S_k^x \pm i S_k^y$ in the non-Kramers case [52–57]. The contribution of dipole-dipole interactions is negligible, $\mu_0 \mu_B^2 g_c^2 / (16\pi r_1^3) \sim 0.01 J_{zz}$.
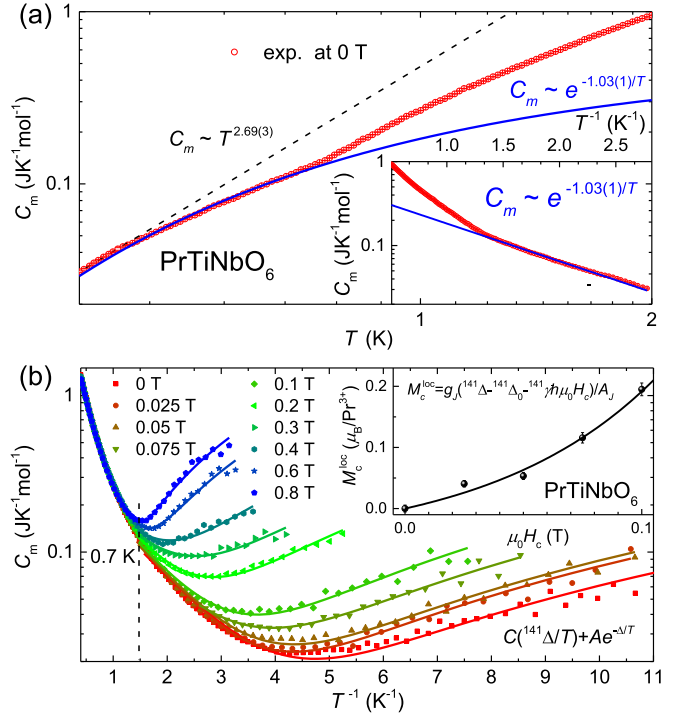

FIG. 7. (a) Low-T magnetic heat capacities of $PrTiNbO_6$ measured at 0 T using the PPMS ^{3}He option. The black dashed line shows the power-law dependence, while the blue solid line represents the exponential fit below 0.7 K. The inset shows the corresponding C_m vs T^{-1} plot. The nuclear contribution is negligible above 0.3 K at 0 T. (b) Magnetic heat capacities of the $PrTiNbO_6$ single crystal measured in magnetic fields applied along the c axis using the home-built setup in a ^{3}He-^{4}He dilution refrigerator, with the colored lines showing the corresponding fits below ~0.7 K. The inset shows field dependence of the local magnetization below 0.1 T with the black line representing an exponential fit.

E. Low-energy spin excitation

We now turn to the spin gap of $PrTiNbO_6$. The exponential behavior of the zero-field magnetic heat capacity is observed at $0.36 \leqslant T \leqslant 0.7$ K. By fitting the data with $C_m \propto \exp(-\Delta_0/T)$, we arrive at $\Delta_0 = 1.03(1)$ K $\sim 0.2 J_{zz}$ [see Fig. 7(a)]. Alternatively, one could fit the data assuming a power-law behavior ($\sim T^\gamma$), but such a fit extends only up to 0.4 K with a large exponent $\gamma = 2.7$, thus confirming the gapped behavior [see Fig. 7(a)]. Moreover, the very small magnetic heat capacity $C_m < 0.004 R \ln 2$ below 0.4 K [see Fig. 7(b)] ensures the formation of a spin gap. Residual spin entropy $S_m \leqslant 0.001 R \ln 2$ indicates that the GS behavior is approached at ~0.3 K. The single-ion CEF excitations show a gapless behavior in the highly diluted samples (see Fig. 4). Thus the gapped behavior of $PrTiNbO_6$ is due to cooperative magnetism, namely, the spin-spin interactions along the chain.

Neither easy-plane nor easy-axis spin-1/2 XXZ chain models [10,58] can account for the gapped and disordered GS observed in $PrTiNbO_6$. This pinpoints the importance of the $J'_{\pm\pm}$ and $J_{\pm\pm}$ terms in Eq. (6). It is worth noting that the $J'_{\pm\pm}$ term breaks the translational symmetry, following zigzag geometry of the spin chain. In this case, an energy gap may open, according to the Haldane conjecture [59–67].

Finally, let us discuss the zero-field heat capacity below 0.3 K. In the absence of the nuclear contribution, magnetic heat capacity should rapidly decrease to zero with decreasing temperature following the exponential behavior, $\sim \exp(-\Delta_0/T)$. However, experimentally it starts increasing at ~ 0.2 K due to nuclear contribution [see Fig. 7(b)]. In external fields applied along the c axis, this tail gradually shifts towards higher temperatures with an effective gyromagnetic ratio,

$$\frac{\gamma_c^{\text{eff}}(\mu_0 H_c)}{2\pi} = \frac{k_B[^{141}\Delta(\mu_0 H_c) - ^{141}\Delta_0]}{h\mu_0 H_c}, \tag{7}$$

where $^{141}\Delta_0$ and $^{141}\Delta(\mu_0 H_c)$ are the energy gaps of the Schottky tails at applied magnetic fields of 0 T and $\mu_0 H_c$, respectively. The value of $\gamma_c^{\text{eff}}(0.8\,\text{T})/(2\pi) \sim 3.9$ GHz/T is one order of magnitude smaller than the gyromagnetic ratio of free electrons and excludes the effect of free (defect) Pr^{3+} electronic spins in general. On the other hand, $\gamma_c^{\text{eff}}/(2\pi)$ is two orders of magnitude larger than the gyromagnetic ratio of free ^{141}Pr nuclear spins, $^{141}\gamma/(2\pi) \equiv 13$ MHz/T, and comparable to the hyperfine coupling constant of Pr^{3+}, $A_J/h \equiv 1093$ MHz [68,69]. Therefore, we expect that the low-T tail in the heat capacity originates from the ^{141}Pr nuclear spins, which are hyperfine coupled to the local magnetization of the Pr^{3+} electronic spins, M_c^{loc}. The similar tails were also reported as zero-field nuclear contribution in other QSL candidates [70,71].

To avoid the possible artifact of the fitting procedure, we fit the low-T magnetic heat capacity with $C_m = C(^{141}\Delta/T) + A\exp(-\Delta/T)$ below ~ 0.7 K only [see Fig. 7(b)], where the first term is the heat capacity of the ^{141}Pr nuclear spins expressed by a two-level model [see Eq. (3)]. The increase in $^{141}\Delta$ under the magnetic field measures the low-T M_c^{loc} by [69]

$$M_c^{\text{loc}} = \frac{g_J}{A_J}(^{141}\Delta - ^{141}\Delta_0 - ^{141}\gamma\hbar\mu_0 H_c), \tag{8}$$

where $^{141}\Delta_0 = 17.2(2)$ mK is the nuclear gap at 0 T [see Fig. 3(b)], and $g_J = 4/5$ is the Landé g factor. Below $\mu_0 H_c = 0.1$ T $\sim 0.1 J_{zz}/(g_c\mu_B)$, M_c^{loc} shows an exponential-like field dependence [see Fig. 7(b)], corroborating the aforementioned gapped behavior. Above 0.1 T, M_c^{loc} depends on the field almost linearly, and at 0.8 T [$\sim 0.6 J_{zz}/(g_c\mu_B)$] nearly reaches the full polarization [72], indicating an enhanced spin susceptibility at low T and above 0.1 T, $\chi_c^{\text{loc}} = 18(1)$ cm^3 mol$^{-1} \sim 4\chi_c$ (1.8 K) [see Fig. 6(a)].

IV. CONCLUSIONS AND OUTLOOK

We reported the formation of a nontrivial magnetic state in the spin-chain compound PrTiNbO$_6$. CEF randomness caused by the site mixing between Ti^{4+} and Nb^{5+} results in the non-Kramers GS quasidoublet of Pr^{3+} with strong Ising anisotropy. The zigzag chains of the pseudospin-1/2 Pr^{3+} ions feature antiferromagnetic couplings $J_{zz} \simeq 4$ K, and reveal a sizable spin gap $\sim 0.2 J_{zz}$. The gap opening may be related to off-diagonal anisotropy terms that alternate along the chain according to its zigzag geometry. Future studies of spin dynamics and spin-spin correlations of PrTiNbO$_6$ are warranted and made possible through the availability of high-quality single crystals. More generally, we establish quasi-1D rare-earth oxides as a playground for exploring magnetism of quantum spin chains.
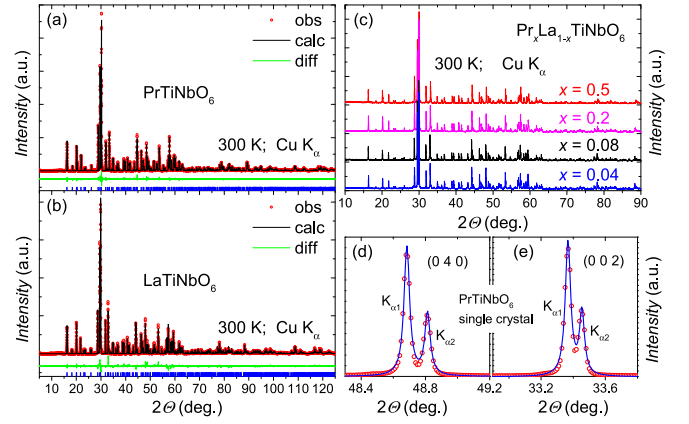

FIG. 8. X-ray powder diffraction and Rietveld refinement patterns (a) for PrTiNbO$_6$ and (b) for LaTiNbO$_6$. (c) X-ray powder diffraction patterns for Pr$_x$La$_{1-x}$TiNbO$_6$ ($x = 0.5$, 0.2, 0.08, and 0.04). Bragg reflections of the PrTiNbO$_6$ single crystal (d) on the ac plane, (0 4 0), with a FWHM $\sim 0.05°$, and (e) on the ab plane, (0 0 2), with a FWHM $\sim 0.05°$.

APPENDIX A: SAMPLE SYNTHESIS AND CHARACTERIZATION

The polycrystalline samples of Pr$_x$La$_{1-x}$TiNbO$_6$ ($x = 1$, 0.5, 0.2, 0.08, 0.04, and 0) were synthesized by a traditional solid-state method. The stoichiometric mixtures of Pr$_6$O$_{11}$, La$_2$O$_3$, TiO$_2$, and Nb$_2$O$_5$ were heated in air up to 1350 °C for 2 days, with an intermediate grinding. An annealing down to 1080 °C was performed for Pr$_x$La$_{1-x}$TiNbO$_6$ ($x = 0.2$, 0.08, 0.04, and 0) in order to obtain the right phase. From $x = 1$ to $x = 0$, the color of the Pr$_x$La$_{1-x}$TiNbO$_6$ powders gradually changes from green to white. Phase purity was confirmed by x-ray diffraction measurements [see Figs. 8(a)–8(c)].

Crystal structures of both PrTiNbO$_6$ and LaTiNbO$_6$ were refined based on the x-ray diffraction data using the Rietveld method implemented in the General Structure Analysis System (GSAS) program [see Figs. 8(a) and 8(b)] [73]. The refined structures are shown in Table I for both PrTiNbO$_6$ and LaTiNbO$_6$, which are consistent with the previously reported results [37–41]. No signatures of preferred orientation were observed [see Figs. 8(a) and 8(b)].

Large-size and high-quality green-colored transparent single crystals of PrTiNbO$_6$ [~ 1 cm, see Fig. 9(a)] were grown in a high-temperature optical floating zone furnace (FZ-T-10000-H-VI-VPM-PC, Crystal Systems Corp.), using 44.4% of the full power of the four lamps (the full power is 1.5 kW for each lamp). The technical details had been reported in our previous growths for YbMgGaO$_4$ and LuMgGaO$_4$ single crystals [28]. The single crystal was oriented by the Laue x-ray diffraction, and was cut consequently by a line cutter

TABLE I. Rietveld-refined crystal structures of $PrTiNbO_6$ and $LaTiNbO_6$ at $\sim$300 K.

Model: $Pnma$		$PrTiNbO_6$	$LaTiNbO_6$
Lattice	a	10.96779(7)	10.94373(9)
Parameters	b	7.52340(5)	7.58623(6)
Å	c	5.38146(4)	5.45202(5)
Pr^{3+} or La^{3+}	x	0.04242(4)	0.04302(6)
$4c$	y	0.25	0.25
	z	0.04091(9)	0.04138(14)
	$U_{iso}(\times 100)$	0.56(2)	0.75(2)
Ti^{4+} / Nb^{5+}	$frac$	0.5	0.5
$8d$	x	0.35550(6)	0.35663(8)
	y	0.00634(8)	0.00545(12)
	z	0.03667(14)	0.03609(20)
	$U_{iso}(\times 100)$	0.45(2)	0.63(3)
$O1^{2-}$	x	0.2874(3)	0.2983(4)
$8d$	y	0.5573(4)	0.5464(5)
	z	0.3706(6)	0.3822(8)
	$U_{iso}(\times 100)$	0.27(6)	0.62(8)
$O2^{2-}$	x	0.0276(3)	0.0313(4)
$8d$	y	0.5374(4)	0.5317(5)
	z	0.2691(5)	0.2669(7)
	$U_{iso}(\times 100)$	0.27(6)	0.62(8)
$O3^{2-}$	x	0.1471(3)	0.1587(5)
$4c$	y	0.25	0.25
	z	0.4539(9)	0.4776(12)
	$U_{iso}(\times 100)$	0.27(6)	0.62(8)
$O4^{2-}$	x	0.3769(4)	0.3777(5)
$4c$	y	0.25	0.25
	z	0.1552(8)	0.1352(10)
	$U_{iso}(\times 100)$	0.27(6)	0.62(8)

along the crystallographic ac plane (ab plane). The properly cut planes (the ac and ab planes) were polished and cross checked by both conventional [Figs. 8(d) and 8(e)] and Laue x-ray diffraction [Figs. 9(b) and 9(c)]. The high quality of the crystal is evidenced by the narrow diffraction peaks, with the full width at half maximum (FWHM), $2\Delta\Theta \sim 0.05°$ [see Figs. 8(d) and 8(e)].
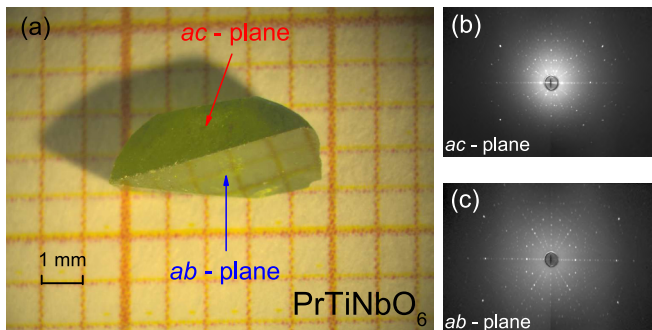

FIG. 9. (a) A single crystal of $PrTiNbO_6$ grown by the floating zone technique. The cut planes, ac plane and ab plane, are marked. Laue x-ray diffraction patterns (b) on the ac plane and (c) on the ab plane.
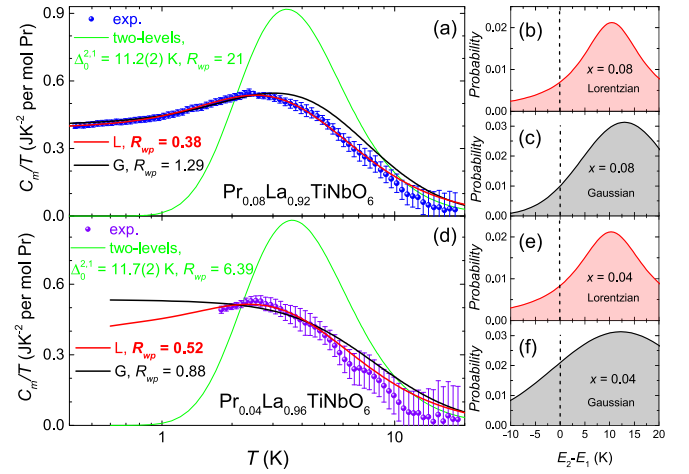

FIG. 10. Magnetic heat capacity measured on (a) $Pr_{0.08}La_{0.92}TiNbO_6$ and (d) $Pr_{0.04}La_{0.96}TiNbO_6$. The green lines show the least-R_{wp} fit by the two-level model without the distribution of E_2-E_1. The red and black lines represent the least-R_{wp} fits with the Lorentzian (L) and Gaussian (G) distribution of E_2-E_1, respectively. The resulting Lorentzian distributions of the spectral weight are shown in (b) and (e) with the fitted parameters $\Delta_0^{2,1} = 10.5$ K and $\omega = 15$ K ($Pr_{0.08}La_{0.92}TiNbO_6$) and $\Delta_0^{2,1} = 10.3$ K and $\omega = 17$ K ($Pr_{0.04}La_{0.96}TiNbO_6$), respectively. The resulting Gaussian distributions of the spectral weight are shown in (c) and (f) with the fitted parameters $\Delta_0^{2,1} = 13.0$ K and $\omega = 20$ K ($Pr_{0.08}La_{0.92}TiNbO_6$) and $\Delta_0^{2,1} = 12.3$ K and $\omega = 32$ K ($Pr_{0.04}La_{0.96}TiNbO_6$), respectively. No internal CEF gap of the ground-state quasidoublet is observed.

APPENDIX B: CEF RANDOMNESS IN $Pr_xLa_{1-x}TiNbO_6$

The fitting procedure using the Lorentzian distribution of E_2-E_1 is described in the main text. We also tried a similar fit with the Gaussian distribution. Similarly, no internal gap between $|E_1\rangle$ and $|E_2\rangle$ is observed [see Figs. 10(c) and 10(f)] from the corresponding least-R_{wp} fits. Furthermore, we also tried to use the Lorentzian model, which allowed a good description of the diluted samples [see Figs. 10(a) and 10(d)], to fit the magnetic heat capacity of $PrTiNbO_6$. However, this single-ion CEF fit is really poor even if the parameters of the Lorentzian distribution are varied [see Fig. 3(d)]. This further confirms that the magnetic heat capacity of $PrTiNbO_6$ cannot be understood in terms of the single-ion CEF physics, and intersite correlations between the Pr^{3+} spins are important.

APPENDIX C: DETAILS OF CEF ANALYSIS

The generic CEF Hamiltonian with the C_{1h} point group symmetry at the Pr^{3+} sites is given by [43–45]

$$\begin{aligned}
\mathcal{H}_{CEF} = \ &B_2^0 O_2^0 + B_2^2 O_2^2 + B_2^{-2} O_2^{-2} + B_4^0 O_4^0 + B_4^2 O_4^2 \\
&+ B_4^{-2} O_4^{-2} + B_4^4 O_4^4 + B_4^{-4} O_4^{-4} + B_6^0 O_6^0 \\
&+ B_6^2 O_6^2 + B_6^{-2} O_6^{-2} + B_6^4 O_6^4 \\
&+ B_6^{-4} O_6^{-4} + B_6^6 O_6^6 + B_6^{-6} O_6^{-6},
\end{aligned} \tag{C1}$$

where B_n^m (m,n are integers and $|m| \leqslant n$) are CEF parameters, and O_n^m are the Stevens operators. The eigenvalues and eigenvectors of Eq. (C1) are given by E_i and $|E_i\rangle$ (i = 1-9), respectively. Under a small external magnetic field of H along

TABLE II. CEF parameters B_n^m obtained from the combined fit. All values are in meV.

B_2^0	B_2^2	B_4^0	B_4^2	B_4^4	B_6^0	B_6^2	B_6^4	B_6^6
1.15	0.93	0.054	0.055	−0.091	−0.00053	−0.0016	−0.0041	−0.0019
		B_2^{-2} $\times 10^8$	B_4^{-2} $\times 10^8$	B_4^{-4} $\times 10^9$	B_6^{-2} $\times 10^9$	B_6^{-4} $\times 10^{10}$	B_6^{-6} $\times 10^{10}$	
		8.3	9.5	7.9	−1.4	−6.8	−5.4	

the a, b, or c axis, the CEF Hamiltonian can be expressed by

$$\mathcal{H}_{\mathrm{CEF}}^{\alpha} = \mathcal{H}_{\mathrm{CEF}} - \mu_0 \mu_B g_J H J_\alpha, \quad \text{(C2)}$$

with $\alpha = x$, y, and z, respectively. The eigenvalues and eigenvectors of Eq. (C2) are given by E_i^α and $|i,\alpha\rangle$, respectively. The single-ion dc magnetic susceptibility can be calculated by

$$\chi_\alpha^{\mathrm{CEF}} = \frac{\mu_B g_J N_A \sum_{i=1}^{9} \exp\left(-\frac{E_i^\alpha}{k_B T}\right) \langle i,\alpha|J_\alpha|i,\alpha\rangle}{H \sum_{i=1}^{9} \exp\left(-\frac{E_i^\alpha}{k_B T}\right)}, \quad \text{(C3)}$$

and the single-ion magnetic heat capacity under 0 T can be calculated by

$$C_m^{\mathrm{CEF}} = \frac{N_A}{k_B T^2} \frac{\partial^2 \ln\left[\sum_{i=1}^{9} \exp\left(-\frac{E_i}{k_B T}\right)\right]}{\partial\left(\frac{1}{k_B T}\right)^2}. \quad \text{(C4)}$$

Through a combined fit using Eqs. (C1)−(C4) to the magnetic susceptibilities and heat capacity measured above 30 K (including the measured pseudospin-1/2 g factors and $\langle E_2 - E_1 \rangle$, see the main text) by minimizing the R_{wp} [see Eq. (4)], all of the CEF parameters B_n^m can be determined experimentally (see Table II). Thus, all the nine eigenvalues (the relative values) and eigenvectors of Eq. (C1) are obtained (see Table III).

The CEF randomness caused by the site mixing between Ti^{4+} and Nb^{5+} [30] merges the two lowest CEF eigenstates, $|E_1\rangle$ and $|E_2\rangle$, into a quasidoublet, because the averaged energy

TABLE III. Fitted CEF energy levels and the corresponding CEF states under 0 T.

$E_1 = 0$ K
$|E_1\rangle = 0.66|3\rangle - 0.66|-3\rangle - 0.24|1\rangle + 0.24|-1\rangle$
$E_2 = 9.4$ K
$|E_2\rangle = 0.71|3\rangle + 0.71|-3\rangle - 0.04|1\rangle - 0.04|-1\rangle$
$E_3 = 125$ K
$|E_3\rangle = -0.07|4\rangle - 0.07|-4\rangle + 0.70|2\rangle + 0.70|-2\rangle - 0.08|0\rangle$
$E_4 = 250$ K
$|E_4\rangle = 0.11|4\rangle - 0.11|-4\rangle - 0.70|2\rangle + 0.70|-2\rangle$
$E_5 = 810$ K
$|E_5\rangle = 0.04|3\rangle + 0.04|-3\rangle + 0.71|1\rangle + 0.71|-1\rangle$
$E_6 = 1000$ K
$|E_6\rangle = 0.32|4\rangle + 0.32|-4\rangle + 0.09|2\rangle + 0.09|-2\rangle + 0.88|0\rangle$
$E_7 = 1040$ K
$|E_7\rangle = 0.24|3\rangle - 0.24|-3\rangle + 0.66|1\rangle - 0.66|-1\rangle$
$E_8 = 1680$ K
$|E_8\rangle = 0.70|4\rangle - 0.70|-4\rangle + 0.11|2\rangle - 0.11|-2\rangle$
$E_9 = 1840$ K
$|E_9\rangle = 0.62|4\rangle + 0.62|-4\rangle + 0.04|2\rangle + 0.04|-2\rangle - 0.46|0\rangle$

difference $\langle E_2 - E_1 \rangle \sim 10$ K, is smaller than the width of the distribution, ~ 16 K. The pseudospin-1/2 magnetic moments can be calculated by

$$m_\alpha^{i,j} = \mu_B g_J \langle E_i|J_\alpha|E_j\rangle, \quad \text{(C5)}$$

under the subspace of $|E_1\rangle$ and $|E_2\rangle$,

$$m_x = m_y = \begin{pmatrix} 0 & 0 \\ 0 & 0 \end{pmatrix}, \quad \text{(C6)}$$

$$m_z = \mu_B \begin{pmatrix} 0 & 2.27 \\ 2.27 & 0 \end{pmatrix}. \quad \text{(C7)}$$

The final CEF ground-state quasidoublet is,

$$|\sigma_\pm\rangle = \frac{1}{\sqrt{2}}(|E_1\rangle \pm |E_2\rangle), \quad \text{(C8)}$$

with the Ising moments along the c axis, ± 2.27 μ_B, respectively ($g_a^{\mathrm{CEF}} = g_b^{\mathrm{CEF}} = 0$ and $g_c^{\mathrm{CEF}} \sim 4.53$).

[1] F. D. M. Haldane, Luttinger liquid theory of one-dimensional quantum fluids. I. Properties of the Luttinger model and their extension to the general 1D interacting spinless Fermi gas, J. Phys. C: Solid State Phys. **14**, 2585 (1981).

[2] L. D. Faddeev and L. A. Takhtajan, What is the spin of a spin wave? Phys. Lett. A **85**, 375 (1981).

[3] A. K. Kolezhuk and H. J. Mikeska, Non-Haldane Spin-Liquid Models with Exact Ground States, Phys. Rev. Lett. **80**, 2709 (1998).

[4] L. Balents, Spin liquids in frustrated magnets, Nature (London) **464**, 199 (2010).

[5] P. A. Lee, An end to the drought of quantum spin liquids, Science **321**, 1306 (2008).

[6] X.-G. Wen, *Quantum Field Theory of Many-Body Systems: From the Origin of Sound to an Origin of Light and Electrons* (Oxford University Press, Oxford, 2004).

[7] E. Lieb, T. Schultz, and D. Mattis, Two soluble models of an antiferromagnetic chain, Ann. Phys. **16**, 407 (1961).

[8] F. D. M. Haldane, Exact Jastrow-Gutzwiller Resonating-Valence-Bond Ground State of the Spin-1/2 Antiferromagnetic Heisenberg Chain with $1/r^2$ Exchange, Phys. Rev. Lett. **60**, 635 (1988).

[9] T. Giamarchi, *Quantum Physics in One Dimension* (Oxford University Press, Oxford, 2004).

[10] A. Imambekov, T. L. Schmidt, and L. I. Glazman, One-dimensional quantum liquids: Beyond the Luttinger liquid paradigm, Rev. Mod. Phys. **84**, 1253 (2012).

[11] T. Hikihara, A. Furusaki, and S. Lukyanov, Dimer correlation amplitudes and dimer excitation gap in spin-$\frac{1}{2}$ XXZ and Heisenberg chains, Phys. Rev. B **96**, 134429 (2017).

[12] S. Takayoshi and M. Sato, Coefficients of bosonized dimer operators in spin-1/2 XXZ chains and their applications, Phys. Rev. B **82**, 214420 (2010).

[13] N. Motoyama, H. Eisaki, and S. Uchida, Magnetic Susceptibility of Ideal Spin 1/2 Heisenberg Antiferromagnetic Chain Systems, Sr_2CuO_3 and $SrCuO_2$, Phys. Rev. Lett. **76**, 3212 (1996).

[14] M. Azuma, Y. Fujishiro, M. Takano, M. Nohara, and H. Takagi, Switching of the gapped singlet spin-liquid state to an antiferromagnetically ordered state in Sr $(Cu_{1-x}Zn_x)_2O_3$, Phys. Rev. B **55**, R8658(R) (1997).

[15] C. P. Landee and M. M. Turnbull, Recent developments in low-dimensional copper (II) molecular magnets, Eur. J. Inorg. Chem. **2013**, 2266 (2013).

[16] M. Hase, I. Terasaki, and K. Uchinokura, Observation of the Spin-Peierls Transition in Linear Cu^{2+} (Spin-1/2) Chains in an Inorganic Compound $CuGeO_3$, Phys. Rev. Lett. **70**, 3651 (1993).

[17] M. Isobe, E. Ninomiya, A. N. Vasil'ev, and Y. Ueda, Novel phase transition in spin-1/2 linear chain systems: $NaTiSi_2O_6$ and $LiTiSi_2O_6$, J. Phys. Soc. Jpn. **71**, 1423 (2002).

[18] C. Heid, H. Weitzel, P. Burlet, M. Bonnet, W. Gonschorek, T. Vogt, J. Norwig, and H. Fuess, Magnetic phase diagram of $CoNb_2O_6$: A neutron diffraction study, J. Magn. Magn. Mater. **151**, 123 (1995).

[19] I. Maartense, I. Yaeger, and B. M. Wanklyn, Field-induced magnetic transitions of $CoNb_2O_6$ in the ordered state, Solid State Commun. **21**, 93 (1977).

[20] T. Hanawa, K. Shinkawa, M. Ishikawa, K. Miyatani, K. Saito, and K. Kohn, Anisotropic specific heat of $CoNb_2O_6$ in magnetic fields, J. Phys. Soc. Jpn. **63**, 2706 (1994).

[21] Z. He, J. Yamaura, Y. Ueda, and W. Cheng, CoV_2O_6 single crystals grown in a closed crucible: unusual magnetic behaviors with large anisotropy and 1/3 magnetization plateau, J. Am. Chem. Soc. **131**, 7554 (2009).

[22] M. Mekata and K. Adachi, Magnetic structure of $CsCoCl_3$, J. Phys. Soc. Jpn. **44**, 806 (1978).

[23] H. Yoshizawa and K. Hirakawa, Neutron scattering study of a one-dimensional Ising-like antiferromagnet $CsCoCl_3$. I. Instantaneous correlation, J. Phys. Soc. Jpn. **46**, 448 (1979).

[24] Z. He, D. Fu, T. Kyômen, T. Taniyama, and M. Itoh, Crystal growth and magnetic properties of $BaCo_2V_2O_8$, Chem. Mater. **17**, 2924 (2005).

[25] Z. He, T. Taniyama, and M. Itoh, Antiferromagnetic-paramagnetic transitions in longitudinal and transverse magnetic fields in a $SrCo_2V_2O_8$ crystal, Phys. Rev. B **73**, 212406 (2006).

[26] Z. Wang, J. Wu, W. Yang, A. K. Bera, D. Kamenskyi, A. T. M. Nazmul Islam, S. Xu, J. M. Law, B. Lake, C. Wu, and A. Loidl, Experimental observation of Bethe strings, Nature **554**, 219 (2018).

[27] Y. Li, H. Liao, Z. Zhang, S. Li, F. Jin, L. Ling, L. Zhang, Y. Zou, L. Pi, Z. Yang *et al.*, Gapless quantum spin liquid ground state in the two-dimensional spin-1/2 triangular antiferromagnet $YbMgGaO_4$, Sci. Rep. **5**, 16419 (2015).

[28] Y. Li, G. Chen, W. Tong, L. Pi, J. Liu, Z. Yang, X. Wang, and Q. Zhang, Rare-Earth Triangular Lattice Spin Liquid: A Single-Crystal Study of $YbMgGaO_4$, Phys. Rev. Lett. **115**, 167203 (2015).

[29] Y. Li, D. Adroja, P. K. Biswas, P. J. Baker, Q. Zhang, J. Liu, A. A. Tsirlin, P. Gegenwart, and Q. Zhang, Muon Spin Relaxation Evidence for the $U(1)$ Quantum Spin-Liquid Ground State in the Triangular Antiferromagnet $YbMgGaO_4$, Phys. Rev. Lett. **117**, 097201 (2016).

[30] Y. Li, D. Adroja, R. I. Bewley, D. Voneshen, A. A. Tsirlin, P. Gegenwart, and Q. Zhang, Crystalline Electric-Field Random-

ness in the Triangular Lattice Spin-Liquid $YbMgGaO_4$, Phys. Rev. Lett. **118**, 107202 (2017).

[31] Y. Li, D. Adroja, D. Voneshen, R. I. Bewley, Q. Zhang, A. A. Tsirlin, and P. Gegenwart, Nearest-neighbor resonating valence bonds in $YbMgGaO_4$, Nat. Commun. **8**, 15814 (2017).

[32] Z. Zhu, P. A. Maksimov, S. R. White, and A. L. Chernyshev, Disorder-Induced Mimicry of a Spin Liquid in $YbMgGaO_4$, Phys. Rev. Lett. **119**, 157201 (2017).

[33] Y. Tokiwa and P. Gegenwart, High-resolution alternating-field technique to determine the magnetocaloric effect of metals down to very low temperatures, Rev. Sci. Instrum. **82**, 013905 (2011).

[34] Quantum Design, PPMS heat capacity option user's manual, Quantum Design (2004).

[35] M. F. Smith, J. Paglione, M. B. Walker, and L. Taillefer, Origin of anomalous low-temperature downturns in the thermal conductivity of cuprates, Phys. Rev. B **71**, 014506 (2005).

[36] See https://www.originlab.com/doc/Origin-Help/Interpret-Regression-Result for adj. R^2.

[37] M. T. Sebastian, S. Solomon, R. Ratheesh, J. George, and P. Mohanan, Preparation, characterization, and microwave properties of $RETiNbO_6$ (RE = Ce, Pr, Nd, Sm, Eu, Gd, Tb, Dy, Y, and Yb) dielectric ceramics, J. Am. Ceram. Soc. **84**, 1487 (2001).

[38] K. P. Surendran, M. R. Varma, P. Mohanan, and M. T. Sebastian, Microwave dielectric properties of $RE_{1-x}RE'_xTiNbO_6$ [RE = Pr, Nd, Sm; RE' = Gd, Dy, Y] ceramics, J. Am. Ceram. Soc. **86**, 1695 (2003).

[39] X. Qi, H. G. Gallagher, T. P. J. Han, and B. Henderson, Modified Czochralski growth and characterization of $RETiNbO_6$ crystals, J. Cryst. Growth **180**, 73 (1997).

[40] X. Qi, R. Illingworth, H. G. Gallagher, T. P. J. Han, and B. Henderson, Potential laser gain media with the stoichiometric formula $RETiNbO_6$, J. Cryst. Growth **160**, 111 (1996).

[41] X. Qi, T. P. J. Han, H. G. Gallagher, B. Henderson, R. Illingworth, and I. S. Ruddock, Optical spectroscopy of $PrTiNbO_6$, $NdTiNbO_6$ and $ErTiNbO_6$ single crystals, J. Phys.: Condens. Matter **8**, 4837 (1996).

[42] T. Moriya, New Mechanism of Anisotropic Superexchange Interaction, Phys. Rev. Lett. **4**, 228 (1960).

[43] K. Feldmann, K. Hennig, L. Kaun, B. Lippold, M. M. Lukina, S. Matthies, W. Matz, and E. Warming, Crystal field levels of Pr^{3+} in $PrFeO_3$ and $PrGaO_3$ determined by inelastic neutron scattering, Phys. Status Solidi B **72**, 817 (1975).

[44] Y. Xiao, M. Zbiri, R. A. Downie, J.-W. G. Bos, Th. Brückel, and T. Chatterji, Inelastic neutron scattering study of crystal field excitations of Nd^{3+} in $NdFeAsO$, Phys. Rev. B **88**, 214419 (2013).

[45] E. Bauer and M. Rotter, *Magnetism of Complex Metallic Alloys: Crystalline Electric Field Effects* (World Scientific, Singapore, 2009).

[46] V. Nekvasil and I. Veltruský, Effective Hamiltonian and ground state properties of rare-earth ions in iron garnets, J. Magn. Magn. Mater. **86**, 315 (1990).

[47] K. Matsuhira, Y. Hinatsu, K. Tenya, H. Amitsuka, and T. Sakakibara, Low-temperature magnetic properties of pyrochlore stannates, J. Phys. Soc. Jpn. **71**, 1576 (2002).

[48] K. Matsuhira, C. Sekine, C. Paulsen, and Y. Hinatsu, Low-temperature magnetic properties of the geometrically frustrated pyrochlore $Pr_2Sn_2O_7$, J. Magn. Magn. Mater. **272**, E981 (2004).

[49] H. D. Zhou, C. R. Wiebe, J. A. Janik, L. Balicas, Y. J. Yo, Y. Qiu, J. R. D. Copley, and J. S. Gardner, Dynamic Spin Ice: $Pr_2Sn_2O_7$, Phys. Rev. Lett. **101**, 227204 (2008).

[50] A. J. Princep, D. Prabhakaran, A. T. Boothroyd, and D. T. Adroja, Crystal-field states of Pr^{3+} in the candidate quantum spin ice $Pr_2Sn_2O_7$, Phys. Rev. B **88**, 104421 (2013).

[51] F. R. Foronda, F. Lang, J. S. Möller, T. Lancaster, A. T. Boothroyd, F. L. Pratt, S. R. Giblin, D. Prabhakaran, and S. J. Blundell, Anisotropic Local Modification of Crystal Field Levels in Pr-Based Pyrochlores: A Muon-Induced Effect Modeled Using Density Functional Theory, Phys. Rev. Lett. **114**, 017602 (2015).

[52] S. Onoda and Y. Tanaka, Quantum Melting of Spin Ice: Emergent Cooperative Quadrupole and Chirality, Phys. Rev. Lett. **105**, 047201 (2010).

[53] S. Onoda and Y. Tanaka, Quantum fluctuations in the effective pseudospin-$\frac{1}{2}$ model for magnetic pyrochlore oxides, Phys. Rev. B **83**, 094411 (2011).

[54] S. Onoda, Effective quantum pseudospin-1/2 model for Yb pyrochlore oxides, J. Phys.: Conf. Ser. **320**, 012065 (2011).

[55] S. B. Lee, S. Onoda, and L. Balents, Generic quantum spin ice, Phys. Rev. B **86**, 104412 (2012).

[56] G. Chen, "Magnetic monopole" condensation of the pyrochlore ice $U(1)$ quantum spin liquid: Application to $Pr_2Ir_2O_7$ and $Yb_2Ti_2O_7$, Phys. Rev. B **94**, 205107 (2016).

[57] Y. Li, S. Bachus, Y. Tokiwa, A. A. Tsirlin, and P. Gegenwart, Absence of zero-point entropy in a triangular Ising antiferromagnet, arXiv:1804.00696 (2018).

[58] A. H. Bougourzi, M. Karbach, and G. Müller, Exact two-spinon dynamic structure factor of the one-dimensional $s = \frac{1}{2}$ Heisenberg-Ising antiferromagnet, Phys. Rev. B **57**, 11429 (1998).

[59] L. N. Bulaevskii, Theory of non-uniform antiferromagnetic spin chains, Sov. Phys. JETP **17**, 684 (1963).

[60] A. Brooks Harris, Alternating linear Heisenberg antiferromagnet: The exciton limit, Phys. Rev. B **7**, 3166 (1973).

[61] M. Kohmoto and H. Tasaki, Hidden $Z_2 \times Z_2$ symmetry breaking and the Haldane phase in the $S = 1/2$ quantum spin chain with bond alternation, Phys. Rev. B **46**, 3486 (1992).

[62] K. Totsuka, Magnetization processes in bond-alternating quantum spin chains, Phys. Lett. A **228**, 103 (1997).

[63] B. W. Southern, J. L. M. Cuéllar, and D. A. Lavis, Multimagnon excitations in alternating spin/bond chains, Phys. Rev. B **58**, 9156 (1998).

[64] S. Paul and A. K. Ghosh, Ground state properties of the bond alternating spin-1/2 anisotropic Heisenberg chain, Condens. Matter Phys. **20**, 23701 (2017).

[65] F. D. M. Haldane, Continuum dynamics of the 1-D Heisenberg antiferromagnet: Identification with the O(3) nonlinear sigma model, Phys. Lett. A **93**, 464 (1983).

[66] F. D. M. Haldane, Nonlinear Field Theory of Large-Spin Heisenberg Antiferromagnets: Semiclassically Quantized Solitons of the One-Dimensional Easy-Axis Néel State, Phys. Rev. Lett. **50**, 1153 (1983).

[67] I. Affleck, Quantum spin chains and the Haldane gap, J. Phys.: Condens. Matter **1**, 3047 (1989).

[68] O. N. Bakharev, A. G. Volodin, A. V. Duglav, A. V. Egorov, M. V. Eremin, A. Yu. Zavidonov, O. V. Lavizina, M. S. Tagirov, and M. A. Teplov, NMR of copper and praseodymium in the two-phase compound $Pr_{1.85}Ce_{0.15}CuO_{4-y}$, Sov. Phys. JETP **74**, 370 (1992).

[69] K. Nehrke and M. W. Pieper, Local Magnetism and Crystal Fields of Pr in $PrBa_2Cu_3O_7$ Studied by ^{141}Pr NMR, Phys. Rev. Lett. **76**, 1936 (1996).

[70] Y. Xu, J. Zhang, Y. S. Li, Y. J. Yu, X. C. Hong, Q. M. Zhang, and S. Y. Li, Absence of Magnetic Thermal Conductivity in the Quantum Spin-Liquid Candidate $YbMgGaO_4$, Phys. Rev. Lett. **117**, 267202 (2016).

[71] S. Yamashita, T. Yamamoto, Y. Nakazawa, M. Tamura, and R. Kato, Gapless spin liquid of an organic triangular compound evidenced by thermodynamic measurements, Nat. Commun. **2**, 275 (2011).

[72] It is not advisable to measure the heat capacity of the $PrTiNbO_6$ single crystal under larger external magnetic fields, as the magnetic anisotropy is too large, $M_c \gg M_a$ or M_b, and the torque may be strong enough to destroy the device.

[73] A. C. Larson and R. B. Von Dreele, GSAS, General Structure Analysis System. LANSCE, MS-H805, Los Alamos, New Mexico (1994).